

Review

# A Short Review of the Effect of Iron Ore Selection on Mineral Phases of Iron Ore Sinter

Junwoo Park , Eunju Kim, In-kook Suh and Joonho Lee \*

Department of Materials Science and Engineering, Korea University, Seoul 02841, Korea; helper0526@korea.ac.kr (J.P.); kukuridie@korea.ac.kr (E.K.); iksuh@korea.ac.kr (I.-k.S.)

\* Correspondence: joonholee@korea.ac.kr

**Abstract:** The sintering process is a thermal agglomeration process, and it is accompanied by chemical reactions. In this process, a mixture of iron ore fines, flux, and coal particles is heated to about 1300 °C–1480 °C in a sinter bed. The strength and reducibility properties of iron ore sinter are obtained by liquid phase sintering. The silico-ferrite of calcium and aluminum (SFCA) is the main bonding phase found in modern iron ore sinters. Since the physicochemical and crystallographic properties of the SFCA are affected by the chemical composition and mineral phases of iron ores, a crystallographic understanding of iron ores and sintered ore is important to enhance the quality of iron ore sinter. Scrap and by-products from steel mills are expected to be used in the iron ore sintering process as recyclable resources, and in such a case, the crystallographic properties of iron ore sinter will be affected using these materials. The objective of this paper is to present a short review on research related to mineral phases and structural properties of iron ore and sintered ore.

**Keywords:** Ironmaking; iron ore; iron ore sinter; silico-ferrite of calcium and aluminum; Rietveld



**Citation:** Park, J.; Kim, E.; Suh, I.-k.; Lee, J. A Short Review of the Effect of Iron Ore Selection on Mineral Phases of Iron Ore Sinter. *Minerals* **2022**, *12*, 35. <https://doi.org/10.3390/min12010035>

Academic Editor: Rajesh Kumar Jyothi

Received: 3 November 2021

Accepted: 22 December 2021

Published: 25 December 2021

**Publisher's Note:** MDPI stays neutral with regard to jurisdictional claims in published maps and institutional affiliations.



**Copyright:** © 2021 by the authors. Licensee MDPI, Basel, Switzerland. This article is an open access article distributed under the terms and conditions of the Creative Commons Attribution (CC BY) license (<https://creativecommons.org/licenses/by/4.0/>).

## 1. Introduction

A crystallographic understanding of iron ores and sintered ore is necessary to produce qualified iron ore sinter. In most Asian countries, iron ore sinters used in ironmaking are produced by mixing iron ores originating from different deposits around the world, such as those in Australia, Brazil, China, and India [1]. During the sintering process, iron ore, flux, and coal particles are mixed together and heated to about 1300 °C–1480 °C in a sinter bed [2–6]. The strength of the iron ore sinter is obtained by calcium ferrite liquid phase sintering. Since iron ores used for producing iron ore sinter can have different chemical compositions and crystallographic characteristics, a crystallographic understanding of iron ores and sintered ore is necessary to guarantee the quality of iron ore sinter. In particular, as demand for the recycling of metallic resources is increasing, the utilization of steel scrap as well as by-products of steel mills is increasing [7–12]. Against this scenario, crystallographic studies of iron ore sinter containing recycled metallic materials have acquired increased relevance.

Iron ore sinter has a complex microstructure and comprises hematite, magnetite, silico-ferrite of calcium and aluminum (SFCA), dicalcium silicate (C2S), etc. The fraction of each phase is determined by the total composition, thermal history, and gas atmosphere during the reaction [13–15], and phase identification and quantitative analysis are performed using automated image analysis, reflected light microscopy, electron probe microanalysis, and Rietveld analysis method [16]. Among them, the Rietveld analysis method would be the most reasonable method for quantitative phase analysis (QPA) and obtaining crystal structure information since image analysis methods are based on limited 2D information. Hamilton et al. introduced the Rietveld method for the first time in their analysis of a single crystal of SFCA X-ray diffraction (XRD) patterns [17]. Recently, Webster et al. investigated the phase transition of iron ore sinter and the formation mechanism of SFCA at high temperatures using in situ synchrotron XRD and QPA [14,18–23]. Many researchers have

used the Rietveld method for the analysis of iron ore and iron ore sinter. In this study, the types of phases and structural characteristics of sintered ore were investigated, and they are systematically reviewed here.

## 2. Mineralogical Analysis of Iron Ores

Various types of iron ores are produced around the world. Table 1 presents mine production and reserves reported by the United States Geological Survey (USGS) in 2021 [1]. According to the USGS's report, global iron ore production reached 2.4 billion tons, mainly from Australia, Brazil, China, and India. Furthermore, iron ore reserves in the world have been estimated at 180 billion tons, with Australia, Brazil, Russia, and China having the most reserves. The difference in the ranking of production and reserves is because of the geographical location of mines and the ease of transportation.

**Table 1.** World mine production and reserves [1] (USGS, 2021 annual report).

	Mine Production (Thousand Metric Tons)	Reserves (Million Metric Tons)
Australia	900,000 (1) *	50,000 (1)
Brazil	400,000 (2)	34,000 (2)
China	340,000(3)	20,000 (4)
India	230,000 (4)	5500 (6)
Russia	95,000 (5)	25,000 (3)
South Africa	71,000 (6)	1000 (8)
Canada	57,000 (7)	6000 (5)
United state	37,000 (8)	3000 (7)
World total	2,400,000	180,000

\* Rankings are listed in ( ).

The quality of raw iron ores is determined mainly based on chemical composition. In particular, the higher the total Fe content, the higher the iron ore grade. Furthermore, low amounts of gangue materials and impurities also result in a high grade. In the present study, the chemical composition of three typical iron ores, namely Mining Area C (MAC), Yandi, and Carajás (supplied by Hyundai Steel), was investigated. Table 2 lists the chemical composition of iron ores produced in various countries [2,4,24–27]. The total Fe content of iron ore varies from 31 to 69 wt%. SiO<sub>2</sub> and Al<sub>2</sub>O<sub>3</sub> are mainly present as gangue components in iron ore, and their content is in the range 0.35–56 and 0.23–6.5 wt%, respectively. Furthermore, sulfur and phosphorus concentrations are in the range of 0.001–0.3 and 0.004–0.87 wt%, respectively. Figure 1 shows a comparison of the chemical composition of iron ores between different countries. High-grade iron ores with total Fe content exceeding 60 wt% [28] are found in Brazil, Canada, and Uganda. In the case of Australia, India, the United States, and Russia, the ore grade is around 60 wt%. In particular, iron ores found in China have a disadvantage in terms of the total Fe content, apart from typically having high SiO<sub>2</sub>, phosphorus, and sulfur content. Iron ores from China may also contain TiO<sub>2</sub>, which may cause TiC formation during blast furnace operation [29]. These geological characteristics of Chinese iron ore originate from the nature of banded iron formation (BIF) [2,4]; in low-rainfall areas, the ore remains unenriched and therefore contains high concentrations of impurities. Iron ores from India and Uganda are characterized by high total Fe and Al<sub>2</sub>O<sub>3</sub> content. In iron ores from Russia, phosphorus and sulfur content are relatively high. Steel mills blend various iron ores to obtain sintered ore of uniform quality.

**Table 2.** Chemical composition of iron ores in different nations.

Mine	Nation	Chemical Composition (Mass %)						Ref.
		Total Fe	SiO <sub>2</sub>	Al <sub>2</sub> O <sub>3</sub>	S	P	TiO <sub>2</sub>	
Goldsworthy	Australia	63.2	4.9	1.6	-	0.035	-	[24]
Goldsworthy	Australia	62.8	6.1	1.5	0.028	0.004	0.1	[2]
Hammersley	Australia	62.7	4.21	2.57	0.015	0.071	0.13	[2]
Hammersley	Australia	62.7	4.2	2.73	0.016	0.059	-	[25]
Mt. Newman	Australia	62.5	5.6	2.6	0.007	0.069	0.11	[2]
Marra Mamba Mining	Australia	61	3.3	1.8	0.039	0.069	0.07	[2]
Area C (MAC) *	Australia	60.08	4.48	2.46	0.025	-	0.002	Present work
Yandi	Australia	59.5	5.03	1.25	0.013	0.039	0.05	[2]
Yandi *	Australia	56.92	6.06	1.53	0.092	-	0.095	Present work
Irvine Island	Australia	54.4	21.3	0.23	0.04	0.01	-	[26]
Itabira	Brazil	68.9	0.35	0.6	0.010	0.030	-	[24]
MBR	Brazil	68.3	1.3	0.9	0.005	0.03	0.04	[2]
MBR	Brazil	67.3	0.79	0.72	0.005	0.030	-	[25]
Carajás	Brazil	67.2	0.6	0.94	0.01	0.037	0.03	[2]
Carajás *	Brazil	65.61	1.77	0.91	0.011	-	0.088	Present work
Carajás	Brazil	65.4	1	1.05	0.010	0.038	-	[26]
Robe river	Canada	57.2	5.6	2.75	0.028	0.04	0.22	[2]
Carol Lake	Canada	64.7	3.9	1	-	0.005	-	[24]
Nanfen	China	63.4	6.28	1.17	0.110	-	-	[4]
Exi	China	42.6	22.32	2.7	0.03	0.87	-	[27]
Guanzhuang	China	38.7	11.6	-	0.11	0.42	-	[4]
Panzhihua	China	33	-	-	-	-	11	[4]
Qidashan	China	31.2	56	-	0.3	<0.03	-	[4]
Bailadila	India	64	2.5	2.5	0.05	0.100	-	[26]
Donimalai	India	63.5	3	3	0.050	0.080	-	[26]
Goa	India	57.8	2.5	6.5	0.020	0.040	-	[24]
Bakal	Russia	60.7	2.4	2	0.030	0.004	-	[24]
Tula	Russia	52.2	10.1	1.25	0.100	0.600	-	[24]
Nyamiyaga	Uganda	69	0.62	0.43	0.001	<0.02	-	[26]
Kyanyamuzinda	Uganda	68.7	0.41	0.35	0.006	0.02	-	[26]
Rushekye	Uganda	68.4	0.96	0.58	<0.001	<0.02	-	[26]
Kamena	Uganda	67.9	0.8	0.65	0.002	0.02	-	[26]
Butare	Uganda	67.5	1.2	1	<0.001	0.05	-	[26]
Kashenyi	Uganda	60.6	5.1	6	0.003	0.02	-	[26]
Reserve Pellet	USA	63	8.1	0.4	0.003	0.025	-	[24]
Mesabi	USA	57.5	10.1	0.7	0.010	0.060	-	[24]
Minnesota	USA	54.3	6.8	0.4	-	0.230	-	[24]

\* Rietveld analysis was conducted on data.

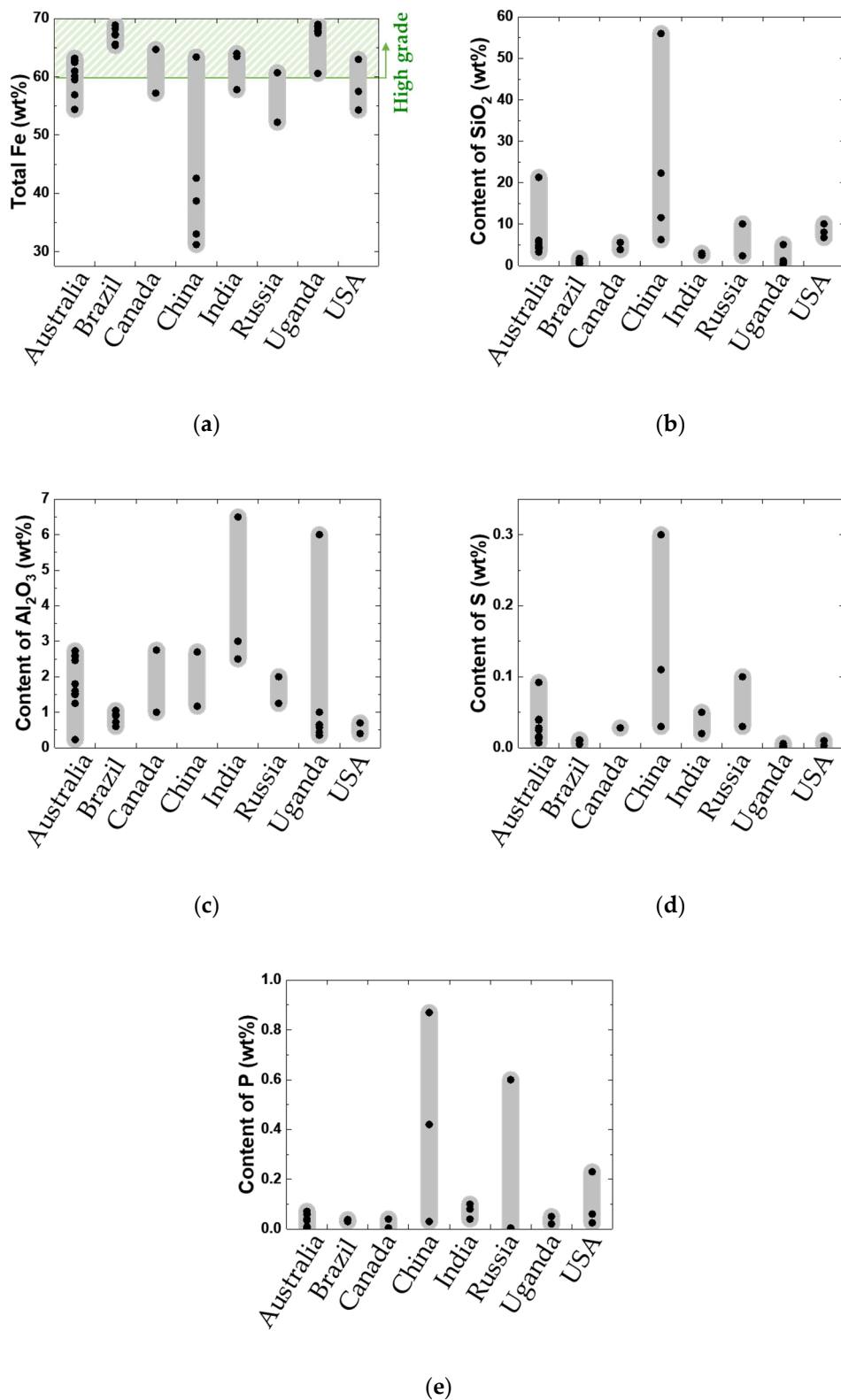


**Figure 1.** Comparison of chemical compositions of iron ores in different nations: (a) Total Fe, (b) SiO<sub>2</sub>, (c) Al<sub>2</sub>O<sub>3</sub>, (d) S, and (e) P content.

Iron ore comprises various mineral phases, which can be categorized into ore and gangue minerals. Typical ore and gangue mineral phases are summarized in Table 3. Hematite, magnetite, and goethite are known to be major ore minerals. SiO<sub>2</sub> and Al<sub>2</sub>O<sub>3</sub>

are major components of gangue materials, such as quartz, kaolinite, and gibbsite. In the present study, Carajás, Yandi, and MAC ores (typical iron ores) were examined using Rietveld analysis and XRD results to determine their mineral phases. Figure 2 shows the XRD and Rietveld analysis results. Table 4 presents the fraction of each phase. Carajás contained 68.11 wt% hematite, 28.95 wt% goethite, and 2.97 wt% quartz. Phases that were present in small amounts were not detected in XRD measurements. By contrast, goethite (77.52 wt%) was the most abundant mineral phase in Yandi. MAC also showed high goethite content (64.1 wt%). Goethite has high loss on ignition (LOI) content, which results in additional energy consumption to remove H<sub>2</sub>O. During the selection of iron ores, apart from the chemical composition, mineral phases should also be considered.

**Table 3.** Common ore minerals and gangue mineral phases in iron ore [4].

Chemical Formula			
Ore Minerals		Gangue Minerals	
Hematite	Fe <sub>2</sub> O <sub>3</sub>	Quartz	SiO <sub>2</sub>
Magnetite	Fe <sub>3</sub> O <sub>4</sub>	Kaolinite	Al <sub>4</sub> (Si <sub>4</sub> O <sub>10</sub> )(OH) <sub>8</sub>
Goethite	FeOOH	Gibbsite	Al(OH) <sub>3</sub>
Maghemite	Fe <sup>3+</sup> [Fe <sup>3+</sup> <sub>1.67</sub> ] <sub>33</sub> O <sub>4</sub>	Minnesotaite	(Mg,Fe <sub>3</sub> ) <sub>3</sub> Si <sub>4</sub> O <sub>10</sub> (OH) <sub>2</sub>
Kenomagnetite	Fe <sub>3-x</sub> ( ) <sub>x</sub> O <sub>4</sub>	Stilpnomelane	(K,Na,Ca) <sub>0.6</sub> (Mg,Fe <sup>2+</sup> ,Fe <sup>3+</sup> ) <sub>6</sub> Si <sub>8</sub> Al(O,OH) <sub>27</sub> 2-4H <sub>2</sub> O
Hydrohematite	Fe <sub>(2-x)/3</sub> (OH) <sub>x</sub> O <sub>3-x</sub>	Chlorite	(Fe,Al,Mg) <sub>3</sub> (Si,Al) <sub>2</sub> O <sub>5</sub> (OH) <sub>4</sub>
		Pyrite	FeS <sub>2</sub>
		Pyrolusite	MnO <sub>2</sub>
		Siderite	FeCO <sub>3</sub>
		Ankerite	Ca(Fe, Mg, Mn)(CO <sub>3</sub> ) <sub>2</sub>

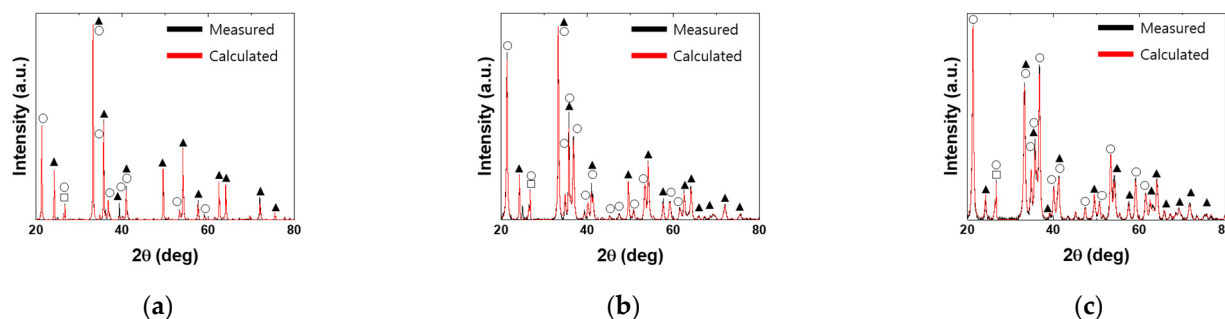


**Figure 2.** X-ray diffraction patterns and Rietveld analysis results: (a) Carajás ore, (b) Yandi ore, and (c) Mining Area C ore (▲: Hematite; ○: Goethite; □: Quartz).

**Table 4.** Phase fractions of iron ores determined through Rietveld analysis (wt%).

Mine	Hematite	Goethite	Quartz
Carajás	68.11	28.95	2.97
Yandi	20.78	77.52	1.70
MAC	33.8	64.1	2.10

### 3. Phase Analysis of Iron Ore Sinter

A blend of iron ores, limestone, and coal was subjected to combustion to obtain iron ore sinter. Figure 3 shows a schematic of the thermal history and formation mechanism of the iron ore sinter. First, CO<sub>2</sub> was removed from limestone by calcination, which yielded CaO. CaO reacted with iron oxides to form calcium ferrites (CF [30], C2F [31], CFA [18], SFCA [17], SFCA-I [32], SFCA-II [33], Fe-rich SFCA [18], etc.), in which gangue materials were assimilated [14,18,20,21,34]. As the sintering temperature reached the maximum,

which was in the range of 1300–1480 °C, a liquid phase was formed [2,4,35,36]. The liquid phase served as a binding material between residual iron oxide particles. When the iron ore sinter was cooled, SFCA, SFCA-I, and other calcium ferrites were formed [37–39]; dicalcium silicate, alumina, quartz, and glass were also present as minor mineral phases. SFCA in the iron ore sinter appeared in different forms (columnar, acicular, prismatic, platy, etc.), depending on the cooling rate. Most of the sinter quality (reducibility and degradation degree) was affected by the amount and shape of SFCA [35,40–47]. As the cooling rate increased, the fractions of columnar and platy type (SFCA, SFCA-I) increased [39]. Furthermore, the fraction of columnar type increased with the  $\text{Al}_2\text{O}_3$  content. Because of the increase in SFCA and SFCA-I, the reducibility of the iron ore sinter improved. MgO inhibited the formation of SFCA [48]. On the other hand, LOI reduced the sintering temperature [49] and thereby decreased the amount of SFCA formed in the iron ore sinter [39]. Some parts of hematite particles were reduced to magnetite during the sintering process, and they were reoxidized during the cooling process, resulting in the formation of secondary hematite. Table 5 shows a compilation of chemical compositions and phase fractions of typical iron ore sinters from the literature.

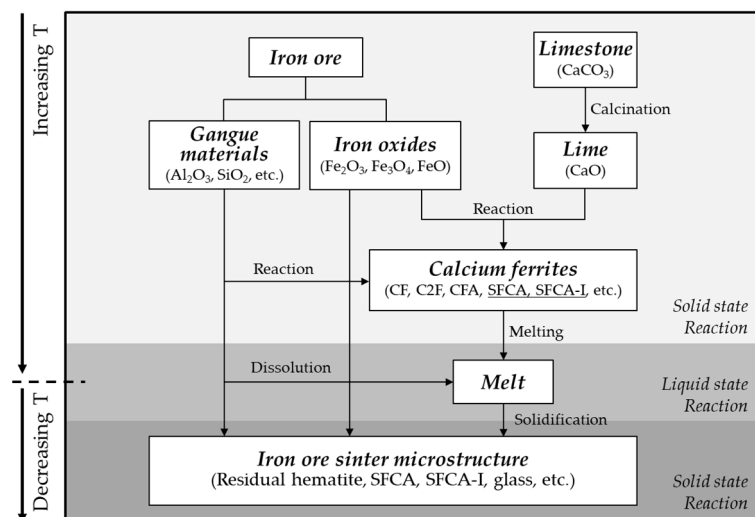


**Figure 3.** Schematic of the formation mechanism of the microstructure of iron ore sinter. Modified from Jeon et al. [13].

Figure 4a shows a typical electron microscope image of the cross-section of a synthetic iron ore sinter reported by Park et al. [50]. Here, SFCA shows a columnar morphology, and it was formed between residual hematite particles. The dark gray color denotes dicalcium silicate (C2S). Figure 5 shows the Rietveld analysis result for sample #6. The sample contained 47.4 wt% SFCA, 29.9 wt%  $\text{Fe}_2\text{O}_3$ , 7.2 wt%  $\text{Fe}_3\text{O}_4$ , 9.1 wt% C2S, 3.7 wt% FeO, and 1.6 wt%  $\text{Al}_2\text{O}_3$ . Other types of calcium ferrites were not detected. Accordingly, it is considered that Rietveld analysis provides detailed information of phase fractions better than the conventional image analysis technique [51–54]. On the other hand, Figure 4b shows a typical photomicrograph of SFCA-I [36]. Apparently, SFCA-I has a platy microstructure that is finer than the microstructure of SFCA.

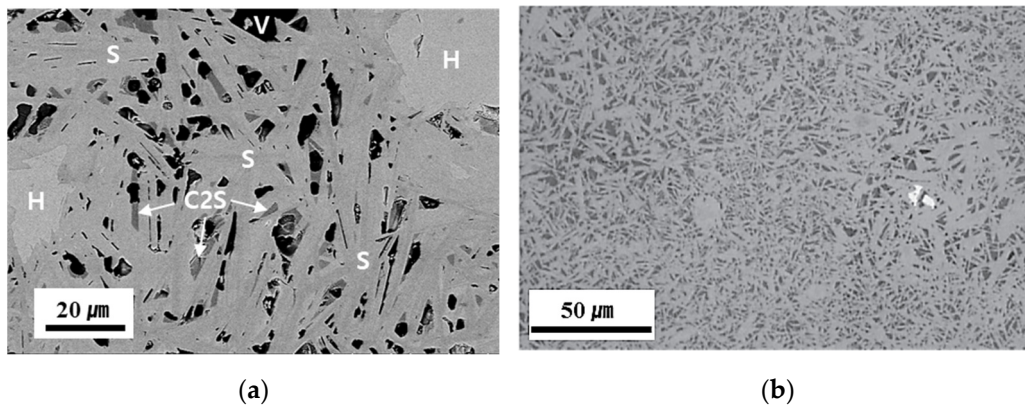


**Figure 4.** Cross-sectional image and an electron micrograph of the synthetic iron ore sinter [36,50]: (a) Sample #8 in Table 5 [50] (V: void; H: hematite; S: silico-ferrite of calcium and aluminum (SFCA); C2S: dicalcium silicate) and (b) the SFCA-I matrix texture [36].

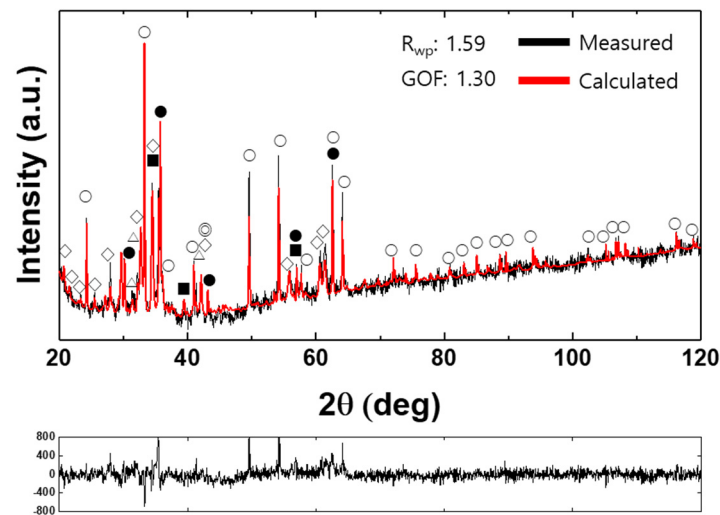


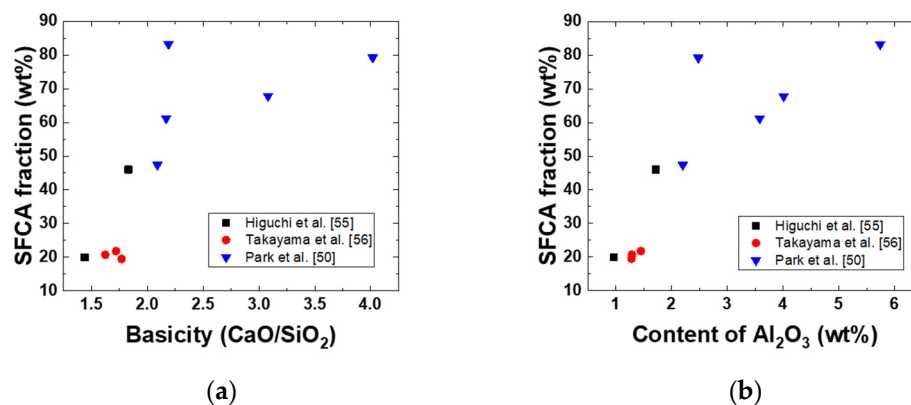
**Figure 5.** Examples of an XRD pattern and a Rietveld analysis result for a synthetic iron ore sinter (Sample #6 in Table 5; ○:  $\text{Fe}_2\text{O}_3$ ; ●:  $\text{Fe}_3\text{O}_4$ ; ◇: SFCA; △: C2S; ⊙: FeO; ■:  $\text{Al}_2\text{O}_3$ ) [50].

In Table 5, chemical compositions and phase fractions of iron ore sinters are listed; the chemical compositions and fractions were determined through Rietveld analysis [50,55,56]. Figure 6 shows the effects of basicity ( $\text{CaO}/\text{SiO}_2$ ) and  $\text{Al}_2\text{O}_3$  content on the SFCA fraction in the iron ore sinter. With increasing basicity or  $\text{Al}_2\text{O}_3$  content, the SFCA fraction increased. However, to obtain a suitable microstructure of the iron ore sinter, the basicity and  $\text{Al}_2\text{O}_3$  content should be optimized.

**Table 5.** Chemical compositions and phase fractions of iron ore sinters (wt%).

No.	Ref.	Chemical Composition				Mineral Phases		
		T.Fe	SiO <sub>2</sub>	Al <sub>2</sub> O <sub>3</sub>	B(CaO/SiO <sub>2</sub> )	Hematite	Magnetite	SFCA
#1	Higuchi et al. [55] *	62.7	3.61	0.96	1.44	51	23	20
#2	Higuchi et al. [55] *	57.7	4.93	1.72	1.83	28	20	46
#3	Takayama et al. [56] **	58.18	5.49	1.28	1.77	44.1	15.5	19.5
#4	Takayama et al. [56] **	56.51	6.75	1.29	1.62	37	18.9	20.7
#5	Takayama et al. [56] **	57.39	6.01	1.45	1.72	33	23	21.8
#6	Park et al. [50] **	54.6	6.22	2.2	2.09	29.9	7.2	47.4
#7	Park et al. [50] **	51.8	4.54	4.01	3.08	8.6	3.1	67.8
#8	Park et al. [50] **	54.6	3.88	2.48	4.02	2.2	1.5	79.2
#9	Park et al. [50] **	53.8	5.88	3.58	2.17	20.4	7.2	61.2
#10	Park et al. [50] **	53	5.86	5.74	2.19	6.3	3.6	83.2

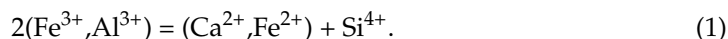
\* Production sinter, \*\* Laboratory sinter.

**Figure 6.** Effects of (a) basicity (CaO/SiO<sub>2</sub>) and (b) Al<sub>2</sub>O<sub>3</sub> content on the SFCA fraction in the iron ore sinter.

#### 4. Chemical Composition of SFCA

In industrial sinters, SFCA has a wide variation of chemical compositions [6,15,17,57–61]. It is useful to use a pseudo-quaternary phase diagram, generally termed as “CCC plane” (Figure 7), to describe a stable composition range for SFCA [17,58–60,62]. Inoue and Ikeda [58] suggested a substitution plane of the end members CaO·3Fe<sub>2</sub>O<sub>3</sub>–CaO·3Al<sub>2</sub>O<sub>3</sub>–CaO·SiO<sub>2</sub>. Dawson et al. [59] reported the substitution plane as CaO·2Fe<sub>2</sub>O<sub>3</sub>–CaO·2Al<sub>2</sub>O<sub>3</sub>–CaO·3SiO<sub>2</sub>, while Hamilton et al. [17] used the CaO·3Fe<sub>2</sub>O<sub>3</sub>–CaO·3Al<sub>2</sub>O<sub>3</sub>–4CaO·3SiO<sub>2</sub> plane, which was accepted by Patrick and Pownceby [62].

Patrick and Powenceby considered that the chemical substitution reaction was as follows:



Here, since a unit cell is considered, a decrease in the number of ions on the left side (Fe<sup>3+</sup> or Al<sup>3+</sup>) should be identical to the increase in the number of ions on the right side (Ca<sup>2+</sup>, Fe<sup>2+</sup>, or Si<sup>4+</sup>). This relationship was confirmed by wet chemical analysis, as shown in Figure 8 [62].

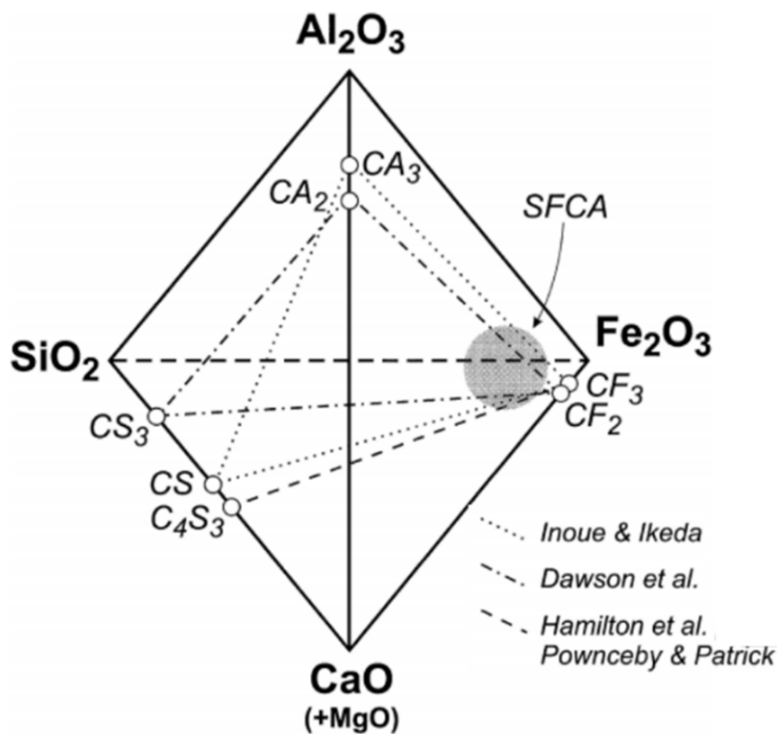


Figure 7. Previously proposed compositional planes for SFCA in the  $Fe_2O_3$ – $Al_2O_3$ – $CaO$ – $SiO_2$  system. The shaded area shows the SFCA compositions in industrial iron ore sinters [62].

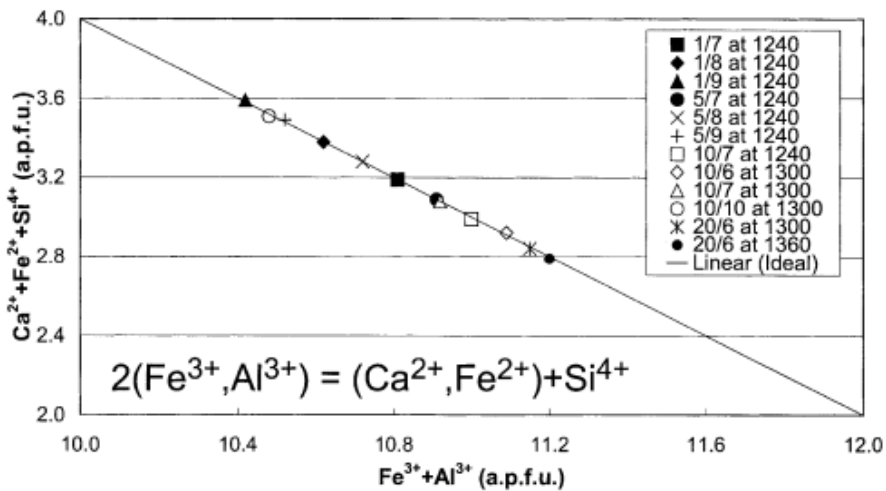
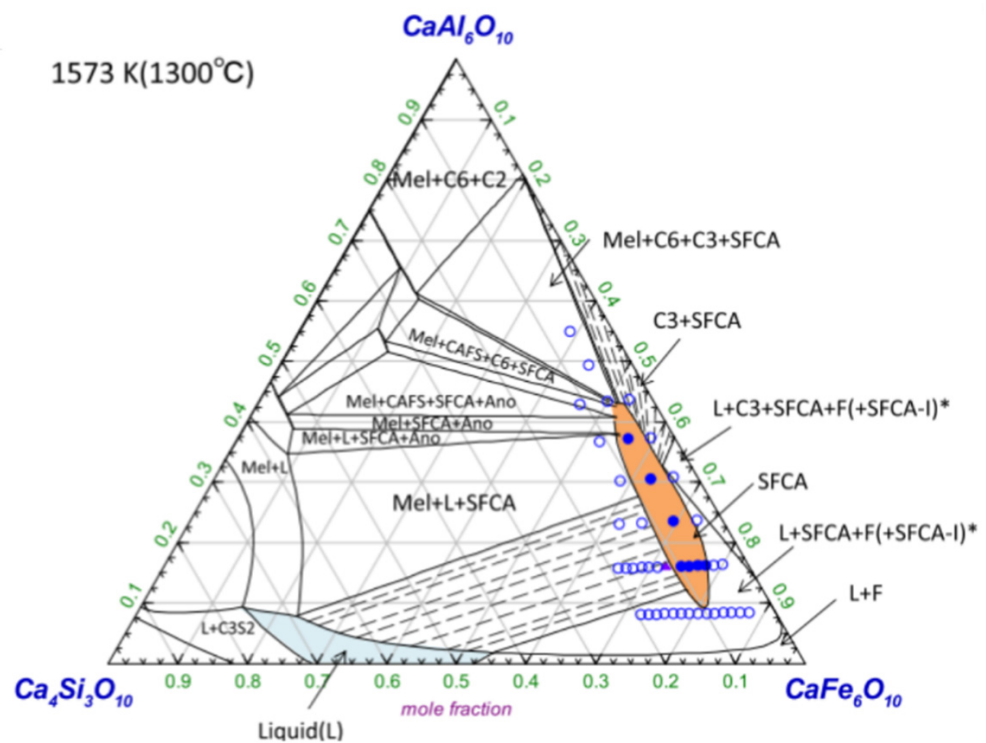


Figure 8. Plot of  $Ca^{2+} + Fe^{2+} + Si^{4+}$  (a.p.f.u.) vs.  $Fe^{3+} + Al^{3+}$  (a.p.f.u.) for various SFCA compositions [62].

Recently, Murao et al. developed a modified quasi-chemical model to describe the thermodynamic property of SFCA [63]. A typical phase diagram of the  $CaO \cdot 3Fe_2O_3$ – $CaO \cdot 3Al_2O_3$ – $4CaO \cdot 3SiO_2$  plane is shown in Figure 9. Clearly, the calculated phase diagram is in reasonable agreement with experimental data.



**Figure 9.** Isothermal phase diagrams of the CA3–CF3–C3S4 system, calculated using a thermodynamic model at 1573 K (filled circles: experimental data points for single-phase SFCA reported by Murao et al. [63]; filled circles: mixtures of SFCA and a meta-stable phase reported by Murao et al. [63]; open circles: a mixture of SFCA and other phases reported by Patrick and Pownceby [62]).

### 5. Crystalline Structure Analysis of SFCA

Rietveld analysis is used to determine crystalline characteristics by matching a theoretical line to a measured XRD profile. SFCA has a triclinic space group and comprises 14 metal atoms and 20 oxygen atoms. Each metal atom is located at an octahedral or a tetrahedral site and is bound to an oxygen atom [17]. Figure 10 shows a schematic of the crystal structure of SFCA; spinel and pyroxene planes are stacked alternately. The unit cell of SFCA has the lattice parameters  $a = 9.061 \text{ \AA}$ ,  $b = 10.020 \text{ \AA}$ , and  $c = 10.920 \text{ \AA}$  (Table 6). Metal atom positions can be categorized as octahedral and tetrahedral sites:  $\text{Ca}^{2+}$ ,  $\text{Fe}^{2+}$ , and  $\text{Mg}^{2+}$  occupy octahedral sites (M1, M2, M3, M7, M10, and M11), while  $\text{Si}^{4+}$ ,  $\text{Fe}^{3+}$ , and  $\text{Al}^{3+}$  occupy tetrahedral sites (M4, M5, M6, M8, M9, and M12). The tetrahedral sites can be categorized into three groups: (1) Fe and Al substitution occurs at the M6 site, (2) Si and Al substitution occurs at the M12 site, and (3) Ca and Fe substitution occurs at the Ca1 site. Sugiyama et al. suggested a Mg-rich SFCAM crystal structure, which was different from the conventional SFCA structure [64,65]. Further studies are required regarding the crystal structure information of Mg-rich SFCAM.

**Table 6.** Main parameters of the crystal structure of SFCA [17] (ICDD: 01-080-0850).

Single Crystal
$a = 9.061 \text{ \AA}$
$b = 10.020 \text{ \AA}$
$c = 10.920 \text{ \AA}$
$\alpha = 60.30^\circ$
$\beta = 73.68^\circ$
$\gamma = 65.81^\circ$

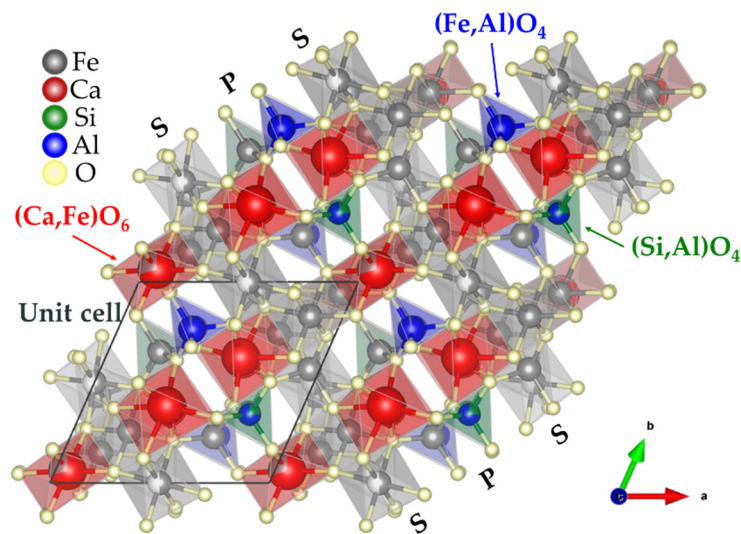


**Figure 10.** Schematic of the crystal structure of SFCA in the polyhedral model (with the ball and stick model) indicating the sequence of spinel (S) and pyroxene (P), and the atom substitution position of the tetrahedral ((Si, Al)O<sub>4</sub>, (Fe, Al)O<sub>4</sub>) and octahedral ((Ca, Fe)O<sub>6</sub>) sites according to Table 7.

**Table 7.** Atomic coordinates and occupancy values for SFCA reported by Hamilton, Takayama et al. and Park et al. [17,50,56].

AtomSite	Hamilton	Takayama et al.	Park et al.
	Ca <sub>2.8</sub> Fe <sub>8.7</sub> Al <sub>1.2</sub> Si <sub>0.8</sub> O <sub>20</sub>	Ca <sub>2.3</sub> Fe <sub>10.3</sub> Al <sub>0.6</sub> Si <sub>0.8</sub> O <sub>20</sub>	Ca <sub>1.6</sub> Fe <sub>11.3</sub> Al <sub>0.2</sub> Si <sub>0.4</sub> Zn <sub>0.4</sub> O <sub>20</sub>
M1	Fe	Fe	Fe
M2	Fe	Fe	Fe
M3	Fe	Fe	Fe
M4	Fe	Fe	Fe
M5	Fe	Fe	Fe
M6	Al	0.4 Al + 0.6 Fe	Fe
M7	Fe	Fe	Fe
M8	Fe	Fe	Fe
M9	Fe	Fe	Fe
M10	0.5 Fe	0.5 Fe	0.5 Fe
M11	0.5 Fe	0.5 Fe	0.5 Fe
Ca1	0.8 Ca + 0.2 Fe	0.3 Ca + 0.7 Fe	Fe
Ca2	Ca	Ca	Ca
Ca3	Ca	Ca	Ca
M12	0.8 Si + 0.2 Al	0.8 Si + 0.2 Al	0.45 Si + 0.2 Al + 0.35 Zn

Recently, Park et al. reported the substitution of Zn at the M12 site in SFCA [50]. They used information on Hamilton’s crystal structure parameters to evaluate the atom occupancy variation. Figure 11 shows metallic atom occupancy changes at the M12 site as a function of the basicity and those at the M6 site with respect to the initial composition of Al<sub>2</sub>O<sub>3</sub>. As the basicity of SFCA increases, Fe occupancy of the M12 site increases, while Si occupancy decreases. When the Al<sub>2</sub>O<sub>3</sub> concentration increases, the Fe occupancy of the M6 site decreases, while Al occupancy increases.

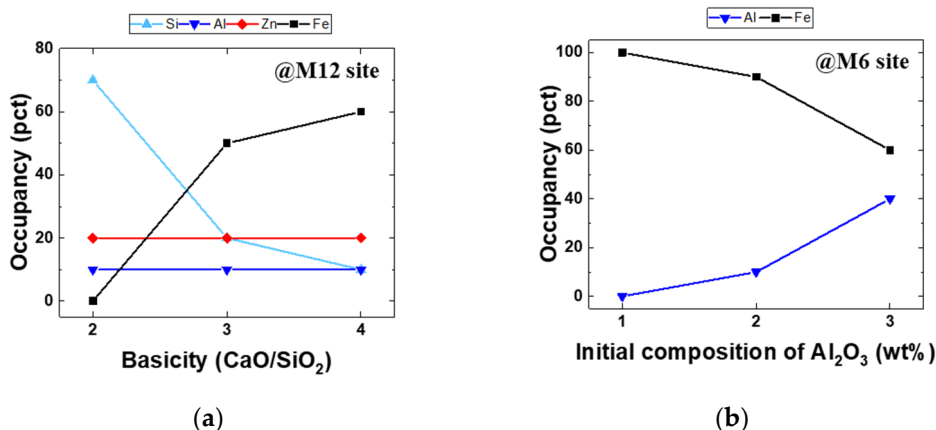


**Figure 11.** Atom occupancy changes at M12 and M6 sites (a) as a function of the basicity and (b) relative to the initial composition of Al<sub>2</sub>O<sub>3</sub> [50].

## 6. Conclusions

In this study, different types of phases and structural characteristics of sintered iron ore were investigated and systematically reviewed. In 2021, global iron ore production reached 2.4 billion tons, with the main producers being Australia, Brazil, China, and India. The total Fe content of iron ore varies from 31 to 69 wt%. Generally, iron ore with total Fe content exceeding about 60 wt% is usually called high-grade iron ore. SiO<sub>2</sub> and Al<sub>2</sub>O<sub>3</sub> are gangue components in iron ore, and their content ranges are 0.35–56 and 0.23–6.5 wt%, respectively. To ensure that the sintered ore they use is of uniform quality, steel mills mix various iron ores. In this study, phases of three typical iron ores (Carajás, Yandi, and MAC) were investigated through Rietveld analysis of XRD results. Hematite, goethite, and quartz were found to be the main mineral phases. Hematite was found in Carajás, and goethite in Yandi and MAC was highest. These ores were mixed to produce a sintered ore, and calcium ferrite melt was formed during the sintering process. The calcium ferrite melt bound iron oxide particles. Some hematite particles were reduced to magnetite during the sintering process, and some were reoxidized during the cooling process to form secondary hematite. In the sintered iron ore, dicalcium silicate, alumina, quartz, and glass were present as minor mineral phases. Calcium ferrite reacted with gangue components to form SFCA. SFCA in the iron ore sinter had columnar or acicular morphology, depending on the cooling rate. Furthermore, the SFCA fraction increased as the basicity or alumina concentration of the sintered iron ore increased. SFCA has a triclinic structure and can be represented as a CA<sub>3</sub>–CF<sub>3</sub>–C<sub>3</sub>S<sub>4</sub> pseudo ternary system. The positions of metallic atoms in SFCA are determined by the substitution reaction  $2(\text{Fe}^{3+}, \text{Al}^{3+}) \leftrightarrow (\text{Ca}^{2+}, \text{Fe}^{2+}) + \text{Si}^{4+}$ . As the basicity of SFCA increases, Fe occupancy of the M12 site increases, while Si occupancy decreases. As the alumina concentration increases, Fe occupancy of the M6 site decreases, while Al occupancy was increases.

**Author Contributions:** Conceptualization, J.P.; methodology, J.P.; software, J.P. and E.K.; validation, J.P., E.K. and I.-k.S.; formal analysis, J.P.; investigation, J.P.; resources, J.P. and E.K.; data curation, J.P.; writing—original draft preparation, J.P.; writing—review and editing, J.P. and I.-k.S.; visualization, J.P.; supervision, J.L.; project administration, J.L.; funding acquisition, J.L. All authors have read and agreed to the published version of the manuscript.

**Funding:** This research was funded by the Ministry of Trade, Industry, and Energy in Korea (20212010100060) and Korea Institute for Advancement of Technology (P0002019).

**Data Availability Statement:** Not applicable.

**Acknowledgments:** This work was supported by the Ministry of Trade, Industry, and Energy in Korea, and the Industrial Strategic Technology Development Program (20212010100060, Development of reduction technology of carbon dioxide from iron making process based on alternative iron source), funded by the Ministry of Trade, Industry, and Energy in Korea. J.P. and E.K. were supported by the Competency Development Program for Industry Specialists of Korea Institute for Advancement of Technology (grant no. P0002019) in Korea.

**Conflicts of Interest:** The authors declare no conflict of interest.

## References

1. USGS. Iron Ore Statistics and Information. Available online: <https://pubs.usgs.gov/periodicals/mcs2021/mcs2021-iron-ore.pdf> (accessed on 24 December 2021).
2. Wakelin, D.H. *The Making, Shaping and Treating of Steel: Ironmaking Volume*; AISE Steel Foundation: Pittsburgh, PA, USA, 1999.
3. Eisele, T.C.; Kawatra, S.K. A review of binders in iron ore pelletization. *Miner. Process. Extr. Met. Rev.* **2003**, *24*, 1–90. [[CrossRef](#)]
4. Lu, L.; Ishiyama, O. 2-Iron ore sintering. In *Iron Ore*; Lu, L., Ed.; Woodhead Publishing: Southton, UK, 2015; pp. 45–84.
5. Mežibrický, R.; Fröhlichová, M.; Findorák, R.; Goettgens, V.S. Ore Assimilation and Secondary Phases by Sintering of Rich and High-Gangue Iron Ores. *Minerals* **2019**, *9*, 128. [[CrossRef](#)]
6. Heikkinen, E.-P.; Iljana, M.; Fabritius, T. Review on the Phase Equilibria in Iron Ore Sinters. *ISIJ Int.* **2020**, *60*, 2633–2648. [[CrossRef](#)]
7. Makkonen, H.T.; Heino, J.; Laitila, L.; Hiltunen, A.; Pöyliö, E.; Härkki, J. Optimisation of steel plant recycling in Finland: Dusts, scales and sludge. *Resour. Conserv. Recycl.* **2002**, *35*, 77–84. [[CrossRef](#)]
8. Hleis, D.; Fernández-Olmo, I.; Ledoux, F.; Kfoury, A.; Courcot, L.; Desmots, T.; Courcot, D. Chemical profile identification of fugitive and confined particle emissions from an integrated iron and steelmaking plant. *J. Hazard. Mater.* **2013**, *250–251*, 246–255. [[CrossRef](#)]
9. Lobato, N.C.C.; Villegas, E.A.; Mansur, M.B. Management of solid wastes from steelmaking and galvanizing processes: A brief review. *Resour. Conserv. Recycl.* **2015**, *102*, 49–57. [[CrossRef](#)]
10. Lanzerstorfer, C.; Bamberger-Strassmayr, B.; Pilz, K. Recycling of Blast Furnace Dust in the Iron Ore Sintering Process: Investigation of Coke Breeze Substitution and the Influence on Off-gas Emissions. *ISIJ Int.* **2015**, *55*, 758–764. [[CrossRef](#)]
11. Lanzerstorfer, C. Electric arc furnace (EAF) dust: Application of air classification for improved zinc enrichment in in-plant recycling. *J. Clean. Prod.* **2018**, *174*, 1–6. [[CrossRef](#)]
12. Lv, W.; Gan, M.; Fan, X.; Ji, Z.; Chen, X.; Yao, J.; Jiang, T. Recycling Utilization of Zinc-Bearing Metallurgical Dust by Reductive Sintering: Reaction Behavior of Zinc Oxide. *JOM* **2019**, *71*, 3173–3180. [[CrossRef](#)]
13. Jeon, J.-W.; Jung, S.-M.; Sasaki, Y. Formation of Calcium Ferrites under Controlled Oxygen Potentials at 1273 K. *ISIJ Int.* **2010**, *50*, 1064–1070. [[CrossRef](#)]
14. Webster, N.; Pownceby, M.; Madsen, I.C.; Kimpton, J.A. Effect of Oxygen Partial Pressure on the Formation Mechanisms of Complex Ca-rich Ferrites. *ISIJ Int.* **2013**, *53*, 774–781. [[CrossRef](#)]
15. Chen, C.; Lu, L.; Jiao, K. Thermodynamic Modelling of Iron Ore Sintering Reactions. *Minerals* **2019**, *9*, 361. [[CrossRef](#)]
16. Honeyands, T.; Manuel, J.; Matthews, L.; O’Dea, D.; Pinson, D.; Leedham, J.; Monaghan, B.; Li, H.; Chen, J.; Hayes, P. Characterising the mineralogy of iron ore sinters—State-of-the-art in Australia. *Proc. Iron Ore* **2017**, 49–60.
17. Hamilton, J.G.; Hoskins, B.; Mumme, W.; Borbidge, W.; Montague, M. The crystal structure and crystal chemistry of Ca<sub>2</sub>. 3Mg<sub>0</sub>. 8Al<sub>1</sub>. 5Si<sub>1</sub>. 1Fe<sub>8</sub>. 3O<sub>20</sub> (SFCA): Solid solution limits and selected phase relationships of SFCA in the SiO<sub>2</sub>-FeO<sub>3</sub>-CaO (-Al<sub>2</sub>O<sub>3</sub>) system. *Neues Jahrbuch für Mineralogie. Abhandlungen* **1989**, *161*, 1–26.
18. Webster, N.A.S.; Pownceby, M.; Madsen, I.C.; Kimpton, J.A. Silico-ferrite of Calcium and Aluminum (SFCA) Iron Ore Sinter Bonding Phases: New Insights into Their Formation During Heating and Cooling. *Met. Mater. Trans. A* **2012**, *43*, 1344–1357. [[CrossRef](#)]
19. Webster, N.; Pownceby, M.; Madsen, I.C. In situ X-ray Diffraction Investigation of the Formation Mechanisms of Silico-Ferrite of Calcium and Aluminium-I-type (SFCA-I-type) Complex Calcium Ferrites. *ISIJ Int.* **2013**, *53*, 1334–1340. [[CrossRef](#)]
20. Webster, N.A.S.; Pownceby, M.; Madsen, I.C.; Studer, A.J.; Manuel, J.R.; Kimpton, J.A. Fundamentals of Silico-Ferrite of Calcium and Aluminum (SFCA) and SFCA-I Iron Ore Sinter Bonding Phase Formation: Effects of CaO:SiO<sub>2</sub> Ratio. *Met. Mater. Trans. A* **2014**, *45*, 2097–2105. [[CrossRef](#)]
21. Webster, N.A.S.; O’Dea, D.P.; Ellis, B.G.; Pownceby, M.I. Effects of Gibbsite, Kaolinite and Al-rich Goethite as Alumina Sources on Silico-Ferrite of Calcium and Aluminium (SFCA) and SFCA-I Iron Ore Sinter Bonding Phase Formation. *ISIJ Int.* **2017**, *57*, 41–47. [[CrossRef](#)]
22. Webster, N.A.S.; Pownceby, M.; Pattel, R.; Manuel, J.R.; Kimpton, J.A. Fundamentals of Silico-Ferrite of Calcium and Aluminium (SFCA) Iron Ore Sinter Bonding Phase Formation: Effects of Basicity and Magnesium on Crystallisation during Cooling. *ISIJ Int.* **2019**, *59*, 263–267. [[CrossRef](#)]
23. Webster, N.A.S.; Pownceby, M.; Pattel, R.; Manuel, J.R.; Kimpton, J.A. Fundamentals of Silico-Ferrite of Calcium and Aluminium (SFCA) Iron Ore Sinter Bonding Phase Formation: Effects of Titanium on Crystallisation during Cooling. *ISIJ Int.* **2019**, *59*, 1007–1010. [[CrossRef](#)]

24. Biswas, A. *Principles of Blast Furnace Iron Making*; Cootha: Calcutta, India, 2005.
25. Cores, A.; Babich, A.; Muniz, M.; Isidro, A.; Ferreira, S.; Martin, R. Iron ores, fluxes and tuyere injected coals used in the blast furnace. *Ironmak. Steelmak.* **2007**, *34*, 231–240. [[CrossRef](#)]
26. Muwanguzi, A.J.B.; Karasev, A.V.; Byaruhanga, J.K.; Jönsson, P.G. Characterization of Chemical Composition and Microstructure of Natural Iron Ore from Muko Deposits. *ISRN Mater. Sci.* **2012**, *2012*, 1–9. [[CrossRef](#)]
27. Song, S.-X.; Campos-Toro, E.F.; Zhang, Y.-M.; Lopez-Valdivieso, A. Morphological and mineralogical characterizations of oolitic iron ore in the Exi region, China. *Int. J. Miner. Met. Mater.* **2013**, *20*, 113–118. [[CrossRef](#)]
28. Geerdes, M.; Toxopeus, H.; van der Vliet, C.; Chaigneau, R.; Vander, T.; Wise, J. *Modern Blast Furnace Ironmaking: An Introduction*; IOS Press: Amsterdam, The Netherlands, 2009.
29. Liao, J.L.; Li, J.; Wang, X.D.; Zhang, Z.T. Influence of TiO<sub>2</sub> and basicity on viscosity of Ti bearing slag. *Ironmak. Steelmak.* **2012**, *39*, 133–139. [[CrossRef](#)]
30. Decker, B.F.; Kasper, J.S. The structure of calcium ferrite. *Acta Crystallogr.* **1957**, *10*, 332–337. [[CrossRef](#)]
31. Millon, E.; Malaman, B.; Bonazebi, A.; Brice, J.; Gerardin, R.; Evrard, O. Structure cristalline du ferrite hémicalcique CaFe<sub>4</sub>O<sub>7</sub>. *Mater. Res. Bull.* **1986**, *21*, 985–994. [[CrossRef](#)]
32. Mumme, W.G.; Clout, J.M.F.; Gable, R.W. The crystal structure of SFCA-I, Ca<sub>3.18</sub>Fe<sup>3+</sup>14.66Al<sub>1.34</sub>Fe<sup>2+</sup>0.82O<sub>28</sub>, a homologue of the aenigmatite structure type, and new crystal structure refinements of β-CFF, Ca<sub>2.99</sub>Fe<sup>3+</sup>14.30Fe<sup>2+</sup>0.55O<sub>25</sub> and Mg-free SFCA, Ca<sub>2.45</sub>Fe<sup>3+</sup>9.04 Al<sub>1.74</sub>Fe<sup>2+</sup>0.16Si<sub>0.6</sub>O<sub>20</sub>. *Neues Jahrb. Fir Mineral. Abh.* **1998**, *173*, 93–117. [[CrossRef](#)]
33. Mumme, W.G. The crystal structure of SFCA-II, Ca<sub>5</sub>. 1Al<sub>9</sub>. 3Fe<sup>3+</sup>+ 18.7 Fe<sup>2+</sup>+ 0.9 O<sub>48</sub> a new homologue of the aenigmatite structure-type, and structure refinement of SFCA-type, Ca<sub>2</sub>Al<sub>5</sub>Fe<sub>7</sub>O<sub>20</sub>. Implications for the nature of the “ternary-phase solid-solution” previously reported in the CaO–Al<sub>2</sub>O<sub>3</sub>–iron oxide system. *Neues Jahrb. Fur Mineral. Abh.* **2003**, *178*, 307–335.
34. Liao, F.; Guo, X.-M. The Effects of Al<sub>2</sub>O<sub>3</sub> and SiO<sub>2</sub> on the Formation Process of Silico-Ferrite of Calcium and Aluminum (SFCA) by Solid-State Reactions. *Minerals* **2019**, *9*, 101. [[CrossRef](#)]
35. Fernández-González, D.; Ruiz-Bustanza, I.; Mochón, J.; González-Gasca, C.; Verdeja, L.F. Iron Ore Sintering: Quality Indices. *Miner. Process. Extr. Met. Rev.* **2017**, *38*, 254–264. [[CrossRef](#)]
36. Nicol, S.; Chen, J.; Pownceby, M.; Webster, N.A.S. A Review of the Chemistry, Structure and Formation Conditions of Silico-Ferrite of Calcium and Aluminum (‘SFCA’) Phases. *ISIJ Int.* **2018**, *58*, 2157–2172. [[CrossRef](#)]
37. Park, T.J.; Choi, J.S.; Min, D.J. In Situ Observation of Crystallization in CaO–Fe<sub>2</sub>O<sub>3</sub> System with Different Cooling Rates and Chemical Compositions Using Confocal Laser Scanning Microscope. *Metall. Mater. Trans. B* **2018**, *49*, 2174–2181. [[CrossRef](#)]
38. Park, T.J.; Choi, J.S.; Min, D.J. Investigation of the Effects of Al<sub>2</sub>O<sub>3</sub> Content and Cooling Rate on Crystallization in Fe<sub>2</sub>O<sub>3</sub>–CaO–Al<sub>2</sub>O<sub>3</sub> System Using In Situ Confocal Laser Scanning Microscopy. *Steel Res. Int.* **2019**, *90*, 1900001. [[CrossRef](#)]
39. Harvey, T.; Pownceby, M.I.; Chen, J.; Webster, N.A.S.; Nguyen, T.B.T.; Matthews, L.; O’Dea, D.; Honeyands, T. Effect of Temperature, Time, and Cooling Rate on the Mineralogy, Morphology, and Reducibility of Iron Ore Sinter Analogues. *JOM* **2021**, *73*, 345–355. [[CrossRef](#)]
40. Taguchi, N.; Otomo, T.; Tasaka, K. Reduction process of CaO–Fe<sub>2</sub>O<sub>3</sub> binary calcium ferrite and resultant expansion. *Tetsu-to-Hagané* **1983**, *69*, 1409–1416. [[CrossRef](#)]
41. Maeda, T.; Ono, Y. Kinetics of Reduction Step of Wustite to Iron in Gaseous Reduction of Quaternary Calcium Ferrite. *Tetsu-to-Hagane* **1991**, *77*, 1569–1576. [[CrossRef](#)]
42. Matsumura, M.; Hoshi, M.; Kawaguchi, T. Improvement of Sinter Softening Property and Reducibility by Controlling Chemical Compositions. *ISIJ Int.* **2005**, *45*, 594–602. [[CrossRef](#)]
43. Murakami, T.; Kodaira, T.; Kasai, E. Effect of the Reduction of Calcium Ferrite on Disintegration Behavior of Sinter under High Hydrogen Atmosphere. *ISIJ Int.* **2015**, *55*, 1197–1205. [[CrossRef](#)]
44. Pownceby, M.I.; Webster, N.; Manuel, J.R.; Ware, N. The influence of ore composition on sinter phase mineralogy and strength. *Miner. Process. Extr. Met.* **2016**, *125*, 140–148. [[CrossRef](#)]
45. Cai, B.; Watanabe, T.; Kamijo, C.; Susa, M.; Hayashi, M. Comparison between Reducibilities of Columnar Silico-ferrite of Calcium and Aluminum (SFCA) Covered with Slag and Acicular SFCA with Fine Pores. *ISIJ Int.* **2018**, *58*, 642–651. [[CrossRef](#)]
46. Ji, Z.; Zhao, Y.; Gan, M.; Fan, X.; Chen, X.; Hu, L. Microstructure and Minerals Evolution of Iron Ore Sinter: Influence of SiO<sub>2</sub> and Al<sub>2</sub>O<sub>3</sub>. *Minerals* **2019**, *9*, 449. [[CrossRef](#)]
47. Kato, K.; Konishi, H.; Ono, H.; Fujimoto, S.; Koizumi, Y. Influence of CaO/SiO<sub>2</sub> on the Reduction Behavior of Sintered Fe<sub>2</sub>O<sub>3</sub>–CaO–SiO<sub>2</sub>–Al<sub>2</sub>O<sub>3</sub> Tablets at the Softening and Melting Temperatures. *ISIJ Int.* **2020**, *60*, 1479–1486. [[CrossRef](#)]
48. Webster, N.A.S.; Pownceby, M.I.; Manuel, J.R.; Pattel, R.; Kimpton, J.A. Fundamentals of Silico-Ferrite of Calcium and Aluminum (SFCA) and SFCA-I Iron Ore Sinter Bonding Phase Formation: Effects of MgO on Phase Formation During Heating. *JOM* **2021**, *73*, 299–305. [[CrossRef](#)]
49. Zhu, D.; Xue, Y.; Pan, J.; Yang, C.; Guo, Z.; Tian, H.; Wang, D.; Shi, Y. An investigation into aluminum occurrence impact on SFCA formation and sinter matrix strength. *J. Mater. Res. Technol.* **2020**, *9*, 10223–10234. [[CrossRef](#)]
50. Park, J.; Rajavaram, R.; Suh, I.-K.; Jeon, J.; Son, S.; Lee, J. Effects of Basicity and Al<sub>2</sub>O<sub>3</sub> Content on the Chemistry of Phases in Iron Ore Sinter Containing ZnO. *Met. Mater. Trans. A* **2020**, *51*, 3016–3027. [[CrossRef](#)]
51. Greco, A.; Jeulin, D.; Serra, J. The Use Of The Texture Analyser To Study Sinter Structure: Application To The Morphology Of Calcium Ferrites Encountered In Basic Sinters Of Rich Iron Ores. *J. Microsc.* **1979**, *116*, 199–211. [[CrossRef](#)]

52. Wang, Z.; Pinson, D.; Chew, S.; Monaghan, B.; Pownceby, M.; Webster, N.; Rogers, H.; Zhang, G. Effects of Sintering Materials and Gas Conditions on Formation of Silico-Ferrites of Calcium and Aluminium during Iron Ore Sintering. *ISIJ Int.* **2016**, *56*, 1138–1147. [[CrossRef](#)]
53. Zhu, D.; Chou, J.; Shi, B.; Pan, J. Influence of MgO on Low Temperature Reduction and Mineralogical Changes of Sinter in Simulated COREX Shaft Furnace Reducing Conditions. *Minerals* **2019**, *9*, 272. [[CrossRef](#)]
54. Honeyands, T.; Manuel, J.; Matthews, L.; O’Dea, D.; Pinson, D.; Leedham, J.; Zhang, G.; Li, H.; Monaghan, B.; Liu, X.; et al. Comparison of the Mineralogy of Iron Ore Sinters Using a Range of Techniques. *Minerals* **2019**, *9*, 333. [[CrossRef](#)]
55. Higuchi, K.; Naito, M.; Nakano, M.; Takamoto, Y. Optimization of Chemical Composition and Microstructure of Iron Ore Sinter for Low-temperature Drip of Molten Iron with High Permeability. *ISIJ Int.* **2004**, *44*, 2057–2066. [[CrossRef](#)]
56. Takayama, T.; Murao, R.; Kimura, M. Quantitative Analysis of Mineral Phases in Iron-ore Sinter by the Rietveld Method of X-ray Diffraction Patterns. *ISIJ Int.* **2018**, *58*, 1069–1078. [[CrossRef](#)]
57. Hancart, J.; Leroy, V.; Bragard, A. A study of the phases present in blast furnace sinter. Some considerations on the mechanism of their formation. *CNRM Metall. Rep.* **1967**, *11*, 3–7.
58. Inoue, K.; Ikeda, T. The Solid Solution State and the Crystal Structure of Calcium Ferrite Formed in Lime-fluxed Iron Ores. *Tetsu-to-Hagane* **1982**, *68*, 2190–2199. [[CrossRef](#)]
59. Dawson, P.; Ostwald, J.; Hayes, K. Calcium ferrites in the new low-silica sintering technology. *BHP Tech. Bull.* **1983**, *27*, 47–51.
60. Pownceby, M.I.; Patrick, T.R. Stability of SFC (silico-ferrite of calcium) solid solution limits, thermal stability and selected phase relationships within the Fe<sub>2</sub>O<sub>3</sub>-CaO-SiO<sub>2</sub> (FCS) system. *Eur. J. Mineral.* **2000**, *12*, 455–468. [[CrossRef](#)]
61. Koryttseva, A.; Webster, N.A.S.; Pownceby, M.; Navrotsky, A. Thermodynamic stability of SFCA (silico-ferrite of calcium and aluminum) and SFCA-I phases. *J. Am. Ceram. Soc.* **2017**, *100*, 3646–3651. [[CrossRef](#)]
62. Patrick, T.R.C.; Pownceby, M.I. Stability of silico-ferrite of calcium and aluminum (SFCA) in air-solid solution limits between 1240 °C and 1390 °C and phase relationships within the Fe<sub>2</sub>O<sub>3</sub>-CaO-Al<sub>2</sub>O<sub>3</sub>-SiO<sub>2</sub> (FCAS) system. *Met. Mater. Trans. A* **2002**, *33*, 79–89. [[CrossRef](#)]
63. Murao, R.; Harano, T.; Kimura, M.; Jung, I.-H. Thermodynamic Modeling of the SFCA Phase Ca<sub>2</sub>(Fe, Ca)<sub>6</sub>(Fe, Al, Si)<sub>6</sub>O<sub>20</sub>. *ISIJ Int.* **2018**, *58*, 259–266. [[CrossRef](#)]
64. Mumme, W.G. A note on the relationship of Ca<sub>2</sub>, 3MgO, 8Al<sub>2</sub>O<sub>3</sub>, 5SiO<sub>2</sub>, 1FeO, 3O<sub>2</sub> (SFCA) with aenigmatie group minerals and sapphirine. *Neues Jahrb. Fur Mineral. Abh.* **1988**, *1988*, 359–366.
65. Sugiyama, K.; Monkawa, A.; Sugiyama, T. Crystal Structure of the SFCAM Phase Ca<sub>2</sub>(Ca, Fe, Mg, Al)<sub>6</sub>(Fe, Al, Si)<sub>6</sub>O<sub>20</sub>. *ISIJ Int.* **2005**, *45*, 560–568. [[CrossRef](#)]